Advances in Water Resources 150 (2021) 103882

Contents lists available at ScienceDirect

Advances in Water Resources

journal homepage: www.elsevier.com/locate/advwatres

Fast simulation of two-phase flow in three-dimensional digital images of heterogeneous porous media using multiresolution curvelet transformation

Abdullah Aljasmi, Muhammad Sahimi*

Mork Family Department of Chemical Engineering and Materials Science, University of Southern California, Los Angeles, California 90089-1211, USA

ARTICLE INFO

Keywords:
Two-phase fluid flow
Porous media
Curvelet transformation

ABSTRACT

Advances in instrumentation have made it possible to obtain high-resolution images of heterogeneous porous media. Such advances and the rapid increase in computational power mean that direct numerical simulation of multiphase flow in two- and three-dimensional (3D) images of porous media is feasible and, therefore, models of pore space that represent simplification and approximation of the actual morphology are dispensable. The bottleneck for image-based simulation is its long computation time. We propose an approach for speeding-up simulation of multiphase flow in 3D images of porous media that utilizes curvelet transformations (CTs). The CTs are designed for denoising of images that contain complex curved surfaces, such as those of heterogeneous porous media. This is possible because the morphology of most porous media contain extended correlations, implying that their images carry redundant information that can be eliminated by a suitable CT. As a result, simulation of multiphase flow in the coarser images are far less computationally intensive. The new approach is used to simulate two-phase flow of CO_2 and brine in a 3D image of Berea sandstone. We demonstrate that the results with the CT-processed image are as accurate as those with the original one, while computations are significantly faster by a speedup factor between one and more than two orders of magnitude.

1. Introduction

Although the physics of two-phase flow in heterogeneous porous media is reasonably well-understood (Helmig, 1997; Sahimi, 2011; Blunt, 2017), its efficient simulation is still the subject of active research. In particular, due to societal interest in geological sequestration of CO_2, there is increasing incentive for studying two-phase flow of CO_2 and brine in such porous media as depleted oil or gas reservoirs (Friedlingstein and Solomon, 2005; Metz et al., 2005; Nordbotten and Celia, 2011). Such simulations are either based on the classical continuum formulation of two-phase flows (Bear, 1972), which necessitates supplying the simulator with various properties of the pore space, such as its porosity and permeability, or entails, as the first step, developing or assuming a model of the pore space that represents faithfully its morphology and the complexities that are associated with it.

Up until relatively recently, the most realistic model of a porous medium at laboratory scale was the pore-network model (PNM) in which the pore space, extracted from an image of the medium, was represented by a network of interconnected pore throats and pore bodies, the effective sizes of which were selected according to some representative statistical distributions that can, in principle, be measured or obtained from the image. Based on representation of a pore space by the PNMs, various approaches were developed in order to simulate two-phase flows in porous media. They included a variety of percolation models, ranging from random (see, for example, Sahimi et al., 1986), to correlated (see, for example, Kantzas and Chatzis, 1988) and invasion percolation (for a simple introduction to invasion percolation see Ebrahimi, 2010), site-bond invasion percolation (Sahimi et al., 1998) that considers the effect of both pore bodies and pore throats on the invasion process, detailed pore-to-pore simulations (Piri and Blunt, 2005; Valvatne and Blunt, 2004), and a combination of effective-medium approximation and random percolation (Ghanbarian et al., 2016). These models have been described and discussed comprehensively by Sahimi (2011), Blunt (2017), and Hunt and Sahimi (2017) and, therefore, need not be described here.

There have been tremendous advances in instrumentation, which have made it possible to obtain high-resolution two- or three-dimensional (3D) images of porous media at laboratory scale. Such images have been becoming important tools for characterization of porous media, as they provide, depending on their resolution, detailed information about the morphology of the pore space. The imaging techniques include focused ion-beam scanning electron microscopes (Lemmens et al., 2011), magnetic resonance imaging (Sheppard et al., 2003) and X-ray computed tomography (Kantzas et al., 1992; Arns et al., 2001; 2002; Porter et al., 2010; Iglauer et al., 2010; Berg et al., 2013; Wildenschild et al., 2014). The images have been used to display fluid distributions

* Corresponding author.
E-mail address: moe@usc.edu (M. Sahimi).

https://doi.org/10.1016/j.advwatres.2021.103882
Received 25 September 2020; Received in revised form 5 February 2021; Accepted 21 February 2021
Available online 24 February 2021

in 3D porous media (Sheppard et al., 2003), even under reservoir conditions (Andrew et al., 2015).

With advances in computational power, high-resolution images of porous media offer the opportunity for precise simulation of fluid flow and transport in porous media. If the physical size of the images is larger than the representative elementary volume (REV) - the minimum volume of a porous medium for its properties to be independent of the dimensions - they may be used directly in numerical simulation of fluid flow and transport in porous media (Arns et al., 2001; 2002; Piller et al., 2009; Tahmasebi et al., 2017), as well as adsorption and deformation (Bakhshian et al., 2018).

Despite the great increase in computational power, numerical simulation of fluid flow and transport in the images of porous media is still computationally very expensive. Natural and many synthetic porous media have pores with irregular shapes, with their surface being rough and often a self-affine fractal. The pores' connectivity is also a spatially-distributed property, giving rise to highly tortuous flow and transport paths. Thus, one needs a high-resolution computational grid that represents such complexities accurately.

Simulation of flow in porous media with the lattice-Boltzmann (LB) algorithm (Huang et al., 2015) is still slower than direct numerical simulation based on the Stokes' equation, although progress has recently been made in speeding it up. An et al. (2020) developed a method that integrates the GPU–accelerated volumetric LB method (VLBM) with an upscaling scheme to solve the pore–scale two-phase flow. They utilized the LB simulator to solve both the level–set equation for image segmentation and the governing equations for multiphase flow dynamics. The method accelerates the standard LB simulations significantly. Aside from the LB–based methods, for image-based direct simulation of multiphase flow and transport in porous media, based on the Navier-Stokes equation, to become the standard approach, the speed of the calculations must increase very significantly without losing accuracy (see, for example, Etemad et al., 2017, for a significant effort in this direction).

In this paper we describe an approach for image-based simulation of multiphase flow in 3D porous media. The main idea is to focus on the image, process and denoise it, and remove the complexities that do not contribute significantly to flow and transport in the pore space, and then carry out numerical simulation of multiphase flow in the coarse image. The image is denoised by curvelet transformations (CTs), a powerful method developed specifically for image processing. As we show in this paper, the method increases the speed of computations very significantly, between one and more than two orders of magnitude, while preserving the accuracy of the solution.

The rest of this paper is structured as follows. In Section 2 we describe the essentials of the CTs. Section 3 explains the method for denoising the images. The two-phase flow problem that we study is described in Section 4, followed by the presentation and discussion of the results in Section 5. The efficiency of the computation is discussed in Section 6, while the paper is summarized in the last section.

2. Curvelet transformations

Denoising of an image to obtain its coarse but accurate representation has been an active research field for decades. Daubechies (1988, 1992) and Mallat (1989b,a) advanced the field significantly by introducing multiresolution wavelet transforms (WTs), which decompose an image into a series of high- and low-pass filter bands, and extract the details of its structure in the horizontal, vertical, and diagonal directions. Heterogeneous porous media, particularly 3D ones, are, however, not only highly noisy, but also contain curved pore surfaces. Thus, the three directions that the WTs employ are not enough for extracting adequate amount of information from 3D images. Note, however, that the WTs have been used very fruitfully in upscaling of geological models of heterogeneous porous media (Mehrabi and Sahimi, 1997; Ebrahimi and Sahimi, 2002; 2004; Pancaldi et al., 2007; Rasaei and Sahimi, 2008; 2009; Babaei and King, 2011; Rezapour et al., 2019), in geophysics (for reviews see Kumar and Foufoula-Georgiou, 1997; Grinsted et al., 2004), and in many other applications.

The shortcomings of the WTs motivated the development of the CTs, which were introduced by Donoho (1999) and Candés et al. (2005), and are highly effective in identifying an image's important features along curves, an aspect that is highly important to the processing of images of porous media. The CTs are multiscale transforms that are capable of producing optimal sparse representation of an image by precise representation of the edges along curves with very high directional sensitivity. They have already been used in geoscience (Olhede and Walden, 2004; Herrmann et al., 2007; Neelamani et al., 2008; Dashtian and Sahimi, 2014) for denoising of geophysical data, such as seismic records. Other applications were described by Ma and Plonka (2009).

We first describe CTs for 2D images, after which its extension to 3D will be discussed. Image processing by the CTs is done in the frequency space. Similar to the WTs, one can construct many types of curvelet functions. To do so, two windows are considered. One, $W(r)$, is a radial window with r being the polar coordinate, while the second window, $V(\theta)$, is intended for the angular direction. Both are smooth, nonnegative, and real functions that satisfy,

$$\sum_{j=-\infty}^{\infty} W^2(2^j r) = 1 \,, \quad r \in (3/4, 3/2) \tag{1}$$

$$\sum_{j=-\infty}^{\infty} V^2(\theta - j) = 1 \,, \quad t \in (-1/2, 1/2) \,. \tag{2}$$

Given $W(r)$ and $V(\theta)$, one constructs a third window U_j in the Fourier space, defined by

$$U_j(r,\theta) = 2^{-3j/4} W(2^{-j} r) V(2^{\lfloor j/2 \rfloor}\theta)/(2\pi) \,, \tag{3}$$

with $\lfloor \cdot \rfloor$ indicating the number's integer part. By definition, the domain in which U_j is nonzero is a polar wedge set by $W(r)$ and $V(\theta)$. By varying j, one utilizes U_j with scale-dependent window widths in both directions. To ensure that U_j takes on real values, its symmetric version, namely, $U_j(r,\theta) + U_j(r,\theta+\pi)$, is used.

The *mother curvelet* $\varphi_i(\mathbf{x})$, referred to as such because all the curvelets at scale 2^{-j} are obtained by rotation and translation of $\varphi_i(\mathbf{x})$, is then defined by its Fourier transform,

$$\widehat{\varphi}_i(\omega) = U_j(\omega) \,, \tag{4}$$

where $U_j(\omega_1, \omega_2) = U(\omega)$. Scale-dependent rotation angles, $\theta_l = 2\pi \times 2^{-\lfloor j/2 \rfloor}$ with, $l = 0, 1, \cdots$ and $\theta_l = 0$, and a sequence of the translation parameters with $k = (k_1, k_2) \in Z^2$ are then introduced. Then, the curvelets as a function of $\mathbf{x} = (x_1, x_2)$ at scale 2^{-j}, orientation θ_l, and position $x_k^{(j,l)} = \mathbf{R}_{\theta_l}^{-1}(k_1 \times 2^{-j}, k_2 \times 2^{-j/2})$ are constructed by Donoho (1999), Candés et al., 2005

$$\varphi_{j,l,k}(\mathbf{x}) = \varphi_j \left[\mathbf{R}_{\theta_l} \left(\mathbf{x} - \mathbf{x}_k^{(j,l)} \right) \right] \,, \tag{5}$$

where $\mathbf{R}_{\theta_l}$ represents a rotation by θ_l radians, given by

$$\mathbf{R}_{\theta_l} = \begin{pmatrix} \cos\theta_l & \sin\theta_l \\ -\sin\theta_l & \cos\theta_l \end{pmatrix} \,, \tag{6}$$

with $\mathbf{R}_{\theta_l}^{-1} = \mathbf{R}_{\theta_l}^{\mathrm{T}} = \mathbf{R}_{-\theta_l}$. Here, T denotes the transpose operation.

3. Denoising of images of porous media

Having set up the CTs, we now describe their use for processing of 2D and 3D images of porous media.

3.1. Two-dimensional images

Suppose that a 2D image of a porous medium, a $n \times n$ array of pixels, is represented by $f(\mathbf{x})$. Its CT, usually referred to as the *curvelet coefficients* (CCs) $C_{j,l,k}$, which are completely analogous to wavelet detail

coefficients, are defined by

$$C_{j,l,k} = \langle f, \varphi_{j,l,k} \rangle = \int f(\mathbf{x})\overline{\varphi_{j,l,k}}(\mathbf{x})\, d\mathbf{x}\,, \tag{7}$$

where the overline denotes a complex conjugate. Because the CTs are constructed and used in the frequency domain, by using the Plancherel's theorem we rewrite the integral in Eq. (7) in the frequency domain,

$$\begin{aligned} C_{j,l,k} &:= \frac{1}{(2\pi)^2} \int \hat{f}(\omega)\overline{\hat{\varphi}_{j,l,k}}(\omega) d\omega \\ &= \frac{1}{(2\pi)^2} \int \hat{f}(\omega) U_j(R_{\theta l}\omega) \exp(i\langle \mathbf{x}_k^{j,l}, \omega\rangle)\, d\omega\,. \end{aligned} \tag{8}$$

Moreover, a window W_0 is introduced by,

$$|W_0(r)|^2 = 1 - \sum_{j=0} W(2^{-j}r)|^2\,. \tag{9}$$

Since the goal is to obtain a coarser representation of the image, we also define, in analogy with the WTs for which coarse-scale wavelet detail coefficients are also defined, for $(k_1, k_2) \in Z$ the coarse-scale curvelets by

$$\varphi_{j_0,k}(\mathbf{x}) = \varphi_{j_0}(\mathbf{x} - 2^{-j_0}\mathbf{k})\,, \tag{10}$$

$$\hat{\varphi}_{j_0}(\omega) = 2^{-j_0} W_0(2^{-j_0}|\omega|)\,. \tag{11}$$

The difference with the WTs is that the coarse-scale curvelets are nondirectional, whereas those defined for the WTs are in the aforementioned three directions. A complete CT consists of the fine-scale directional curvelets $(\varphi_{j,l,k})_{j=j_0,l,k}$ and the coarse-scale isotropic $(\Phi_{j_0,k})_k$, which is called the *father wavelet*.

The idea for processing images of porous media by the CTs (or by the WTS, for that matter) and denoising them exploits the physical fact that the morphology of such media contains extended spatial correlations between the pores and grains (see, for example, Knackstedt et al., 2001). Thus, the same correlations exist between the pixels (voxels in 3D) in the images of porous media. The existence of the correlations implies that images contain redundant information, and that their removal will not damage the essential information that the images carry. Once the redundant information is removed, simulation of flow and transport in the resulting coarser images is accelerated very significantly, as we demonstrate shortly.

The denoising exploits the fact that (Starck et al., 2002) the CCs represent a measure of the local complexity of an image, which in a porous medium is due to the pores' rough surface, which is typically a self-affine fractal (see Sahimi, 2011 for a comprehensive discussion) and its correlation with the surrounding pore space. In other words, the CCs represent a measure of roughness or curviness of the pore-grain interface and, due to the extended correlations, the pores next to the interface are also affected. Therefore, the larger the CCs, the more significant is the curviness and, hence, the roughness. Clearly, if the roughness is severe, its contribution to image-based simulation of multiphase flow should be significant. Thus, if we keep only the most curved portions of the pore space, i.e., if we denoise the image, a coarser computational grid should suffice for the simulations.

There are several ways of denoising or compressing an image (Starck et al., 2002), but we choose to take the simplest approach that, as we demonstrate shortly, suffices for our purpose. The approach, which is referred to as thresholding in image processing, consists of the following steps: (i) Curvelet transform the image and compute the CCs $C_{j,l,k}$. (ii) Normalize the CCs by their largest value. (iii) Introduce a threshold $0 \le \varepsilon < 1$, such that if $C_{j,l,k} < \varepsilon$, it is set to zero. In this way, the algorithm generates a sparser representation of the image in the curvelet space, as many of the CCs of the original image are set to zero, while it still contains all the essential information. The numerical value of ε depends on the computation time and resources that one can afford and has access to.

3.2. Three-dimensional images

The CTs were originally developed for 2D images. Their extension to 3D initially encountered some difficulties associated with curved surfaces, but curvelets for some 3D systems have also been developed (Ying et al., 2005; Woiselle et al., 2010). But, for reasons that will be explained in Section 6, in the present paper we use an alternative approach, namely, we divide a $n \times n \times n$ 3D image into n 2D images of size $n \times n$, apply the methodology described in 3.1 to each 2D image, and then stack together the curvelet-transformed 2D denoised images to reconstruct a 3D image. The orientations of the 2D images relative to the original 3D image does not play a significant role, unless the pore space is strongly anisotropic. If strong anisotropy is present, one may use a CT-based anisotropic feature extraction method (Shinde et al., 2017). In the present work we take the 2D images in the planes perpendicular to the direction of macroscopic flow. With the development of fast 3D CTs, the issue of the orientation of the 2D slices relative to the 3D images becomes irrelevant.

Care must, however, be taken to ensure that after curvelet-transforming and thresholding, the transition from one processed 2D slice to the next is seamless, and does not generate any artifacts. To do this, we used an open-access image processing package that does the segmentation and the stacking process. The software is called *Fiji* (Schindelin et al., 2012), which generates directly 3D images from a series of 2D images, and is also designed to automatically address issues that may arise from image thresholding, which is why the software is a very power tool (for more details see, https://imagej.net/Fiji).

3.3. Simulations in the curvelet or real space?

Once the coarser image is developed, one has two options:

(i) One computes the inverse CT of the thresholded image, and carries out numerical simulation of two-phase flow in it, or
(ii) one curvelet transforms the governing flow equations, solves them in the CT space and, then, computes the inverse CT of the numerical results.

The results presented in this paper were obtained with option (i). It can be shown (Aljasmi and Sahimi, 2020) that if procedure (ii) is followed, the speed-up factor for computations will be a factor of four or better, even if the images in the curvelet space is not denoised. Clearly, then, if the image is denoised, and the computations are still carried out in the CT of the denoised image, the speed-up factor will be quite large.

The reason that one has better efficiency even without thresholding is that, in the CT space a coarser computational grid suffices, because many of the CCs of the image are either very small and, thus, do not make significant contributions, or that due to the correlations they are close to those of their neighbors, indicating a relatively smooth local environment, hence allowing use of larger grid blocks.

4. Details of the simulations

We now describe the porous medium whose image we have used in the computations, and explain the computational procedure.

4.1. The porous medium

We utilized a 3D image of Berea sandstone, which is considered a benchmark for testing various computational approaches to simulating multiphase flow in porous media, and has been used extensively in the past (Valvatne and Blunt, 2004; Ramstad et al., 2012; Raeini et al., 2014). The digital and physical sizes of the sample are, respectively, 200^3 voxels and 2.14^3 mm^3. The porosity and absolute permeability of the sample are, respectively, 0.196 and 1368 mD. Fig. 1 presents the image of the sandstone and its 3D coarse version. The size of the image is larger than its corresponding REV.

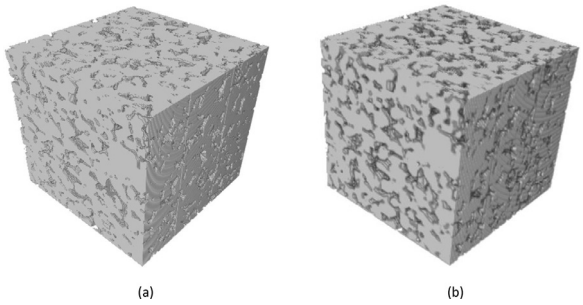

Fig. 1. (a) The original 200^3-voxel image of the Berea sandstone, and (b) the coarse image, obtained with a threshold $\epsilon = 0.8$.

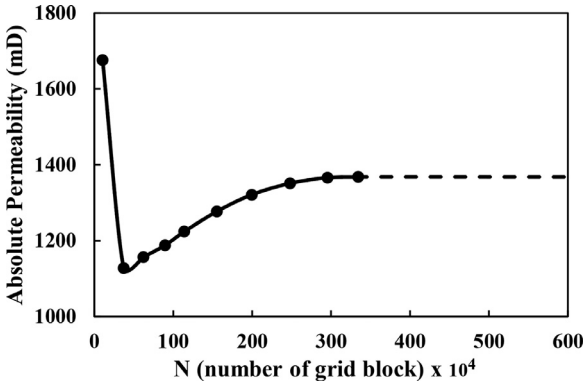

Fig. 2. Dependence of the permeability of the sandstone on the size of the computational grid.

4.2. The governing equations and the numerical simulation procedure

We first carried out simulation of single-phase flow in the image of the Berea sandstone, both in the original one and in the processed images in order to not only estimate the absolute permeability of the pore space, but also determine the size of the computational grid that yield reliable estimate (see below). We then simulated two-phase flow of CO_2 and brine in the same images.

Simulating two-phase flow in porous media requires upscaling the microscopic dynamic and capillary pressures to the Darcy scale. While there are several methods for the upscaling, we used the velocity-weighted averages of both the viscous forces and the pressure gradient that have been demonstrated (Raeini et al., 2014) to yield results that are in agreement with experimental data. As for macroscopic pressure drop ΔP_α in fluid phase α of the two-phase system, we utilized a slightly modified versions of the same equations, which is given by

$$\Delta P_\alpha = -\frac{1}{Q_\alpha}\int \mathbf{v}\cdot[\nabla\cdot(\mu\nabla\mathbf{v})]dV_\alpha\,, \quad \alpha = 1,2\,, \tag{12}$$

where the density ρ and viscosity μ are given by

$$\mu = \phi\mu_1 + (1-\phi)\mu_2\,, \tag{13}$$

$$\rho = \phi\rho_1 + (1-\phi)\rho_2\,. \tag{14}$$

Here, Q_α is the flow rate of phase α, $\mathbf{v}$ is the velocity field, V_α is the portion of pore volume filled with phase α, μ_1 and μ_2 are viscosities of the two fluids, and ϕ is the volume fraction of fluid 1 (brine) in each grid block.

Since the computational grid is Eulerian, one needs a method for including the interfacial tension in grid, so as to reduce numerical diffusion at the interface between the two fluids. Several methods have been proposed for this pupose, such as the continuous surface stress (CSS) (Gueyffier et al., 1999), continuous surface force (CSF), sharp surface force (SSF) (Francois et al., 2006), and filtered surface force (FSF) (Raeini et al., 2012). But the CSF method may generate spurious fluid velocity field that, to some extent, is controlled by the SSF method. To do so, one introduces in the SSF method a sharpened indicator function ϕ of fluid phase 1 that takes on a value of one in fluid 1 (brine) - the wetting fluid - and zero in fluid 2 (CO_2) - the non-wetting fluid - and varies smoothly between the two in the interface region. The approach is capable of controlling the sharpness of the capillary pressure. The FSF approach utilizes a slightly modified indicator function for the interface motion with a capillary force that, compared with the SSF method, is smoother. This compresses the transition zone of the capillary pressure and, hence, resolves the issue with the spurious velocities that may arise. Then, the transition area for capillary pressure is only one grid block. Therefore, we utilized the FSF formulation. The magnitude f of the interfacial force $\mathbf{f}$ is given by

$$f = \kappa\sigma\frac{2\rho}{\rho_w + \rho_{nw}}\nabla\phi\,, \tag{15}$$

with σ being the interfacial tension, and κ the curvature, given by

$$\kappa = -\nabla\cdot\left(\frac{\nabla\phi}{|\nabla\phi|}\right). \tag{16}$$

The governing equation, in addition to the usual mass conservation, is the momentum equation,

$$\frac{\partial}{\partial t}(\rho\mathbf{v}) = -\nabla P + \nabla\cdot(\mu\nabla\mathbf{v}) + \mathbf{f}\,. \tag{17}$$

The indicator function ϕ, indicating the position of the interface between the two fluids, is updated at each time step. This is followed by the calculation of the interfacial force f. Then, the velocity and pressure fields are computed by solving the Stokes' and continuity equations. At steady state Darcy's law for two-phase flow,

$$\mathbf{v}_\alpha = -\frac{k_{r\alpha}K}{\mu_\alpha}\nabla P_\alpha\,, \quad \alpha = 1,2\,, \tag{18}$$

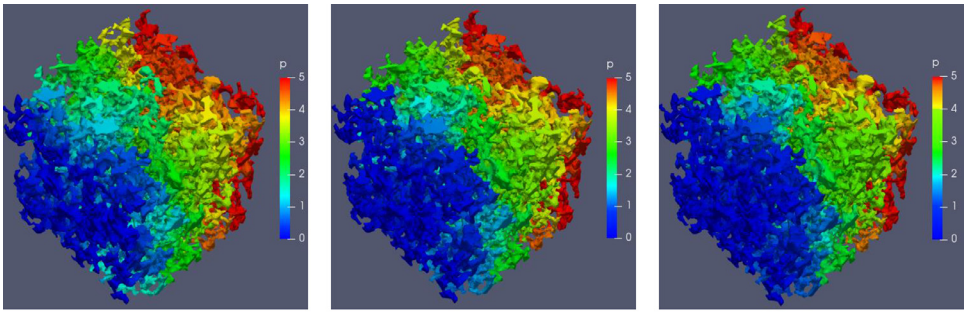

Fig. 3. The pressure distribution at the end of the simulations in (a) the original image; (b) in the denoised images with $\epsilon = 0.5$ and (c) with $\epsilon = 0.9$.

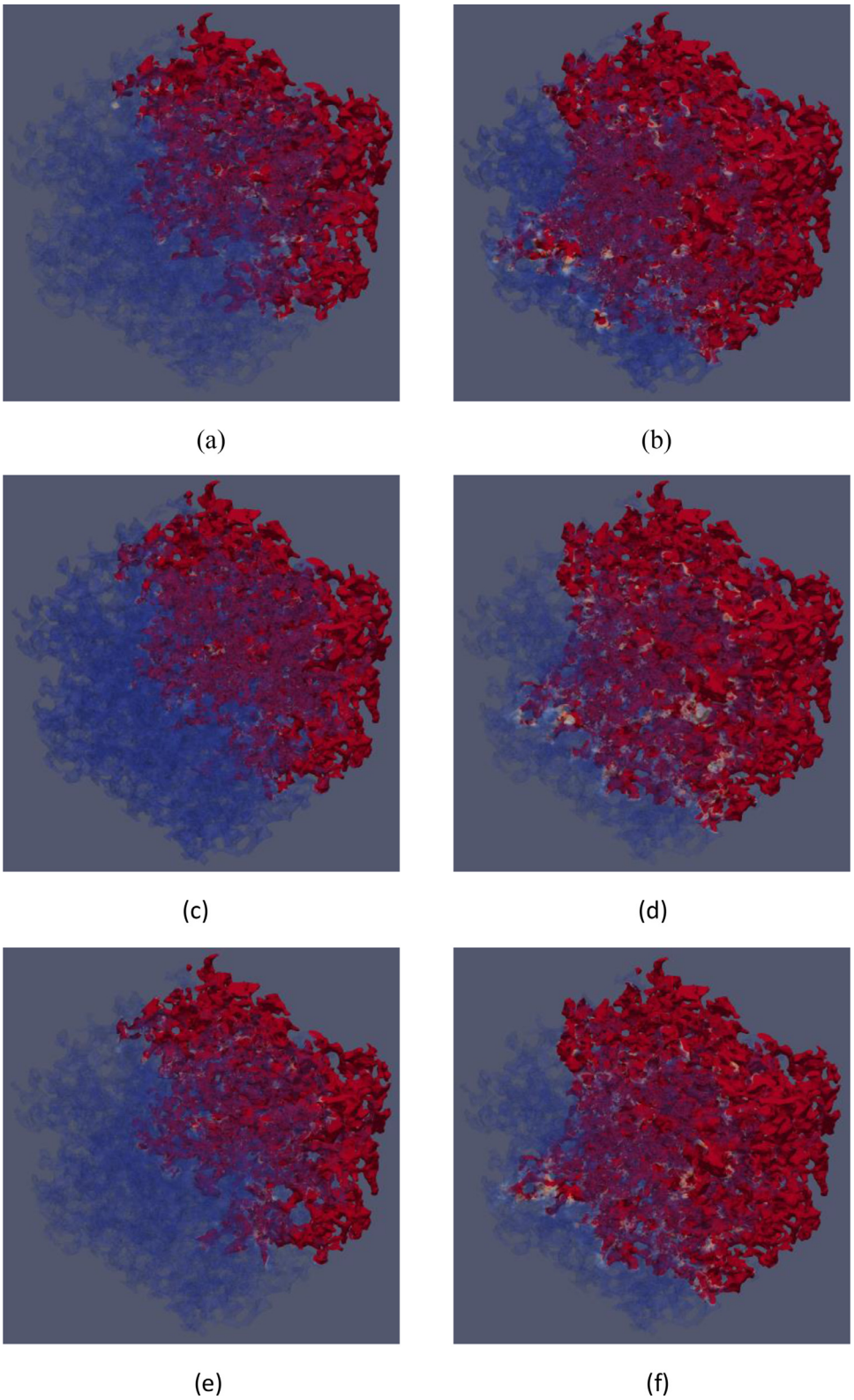

Fig. 4. Evolution of CO_2 distribution (red) in (a) and (b) the original image of the sandstone; (c) and (d) the thresholded image with a threshold $\epsilon = 0.5$, and (e) and (f) the denoised image with $\epsilon = 0.9$, after 30 ms (left) and at the breakthrough time.

is utilized to calculate the relative permeability $k_{r\alpha}$ of fluid phase α as a function of its saturation, where K is the absolute permeability. As for the fluid properties, we used the typical values (Kohanpur et al., 2020): the kinematic viscosities were $\nu_1 = 1.0 \times 10^{-6}$ for brine $\nu_2 = 1.0 \times 10^{-7}$ for CO_2, both in m^2/s, while the densities were $\rho_1 = \rho_2 = 10^3$ kg/m^3. The interfacial tension was assumed to be, $\sigma = 30$ mN/m. The contact angle for the brine was 0°.

The OpenFOAM program (Ubink, 1997) and its modified version (Raeini, 2013), which are open-source softwares that use finite-volume discretization to solve the continuity and the momentum equation in the

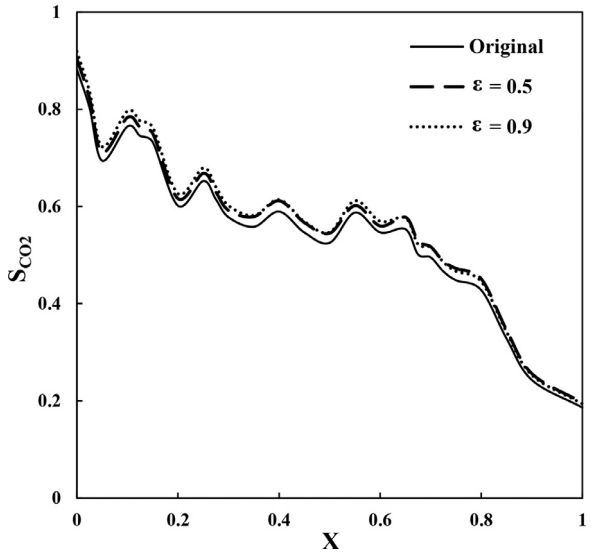

Fig. 5. Saturation profile of CO_2 along the flow direction x at the breakthrough time in the curvelet-transformed images of the sandstone, and its comparison with those in the original image. $X = x/L$ is the normalized distance of the interface from the inlet, where L is the sample's length in the x direction.

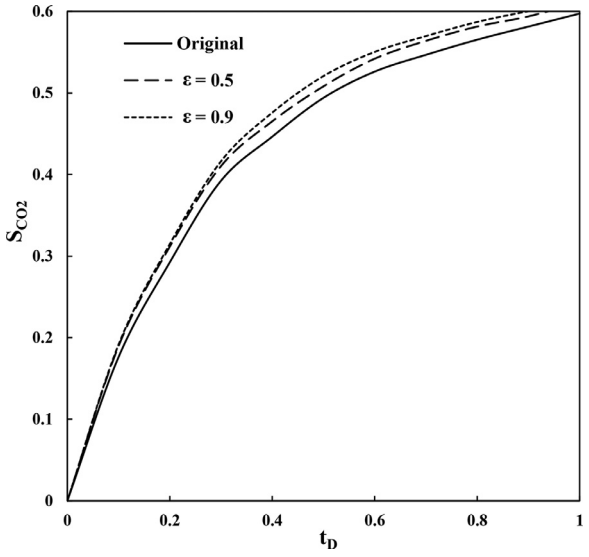

Fig. 6. Evolution of the saturation of CO_2 as a function of the time $t_D = t/t_B$, with t_B being the breakthrough time, in the curvelet-transformed images of the sandstone with two thresholds ϵ and their comparison with those in the original image.

pore space, were utilized for carrying out the numerical simulations. For the two-phase flow simulation two grid blocks per pixel were used. CO_2 was injected into the porous medium with a speed of 4.65×10^{-2} m/s at one face, so that the capillary number was $\mathrm{Ca} = 1.55 \times 10^{-4}$, and a fixed atmospheric pressure was applied at the opposite face. The other four faces were assumed to be impermeable. All the computations were carried out using a HP Spectre x360 computer with a speed of 2GHz and 16 GB of memory.

5. Results

As pointed out earlier, we carried out simulation of both single- and two-phase flows. In what follows we present and discuss the results.

5.1. One-phase flow

We first carried out a series of simulations of single-phase flow, varying the resolution of the computational grid (the number of grid blocks), in order to determine the grid size that yields a permeability independent of the grid's resolution. Fig. 2 presents the results, which indicate that a grid with about 3.34×10^6 blocks is necessary to obtain a stable value of the permeability K, independent of its resolution. The calculated K turned out to be $K = 1368$ mD. We utilized the same grid in the simulation of two-phase flow in the original image without any processing by the CT; see below.

Two thresholds, $\epsilon = 0.5$ and 0.9, were utilized to denoise the image and carry out simulation of single- and two-phase flows. Fig. 3 compares the pressure distributions in the original image and in the two coarser ones. All the essential features of the three distributions are identical. The computed permeabilities are $K = 1443$ and 1467 mD for $\epsilon = 0.5$ and 0.9, respectively. Even the latter estimate with a very high threshold of 0.9 is only 7.3 percent higher than the estimate of K computed with the original image.

5.2. Two-phase flow

Fig. 4 compares the evolution with time of the spatial distribution of CO_2 and brine in the original image of the sandstone with those obtained with the CT-denoised images with the two thresholds. Similar to the pressure distribution in single-phase flow, all the important features of the distributions are completely similar in all the images. More quantitatively, the differences between the saturations in the original images and the thresholded ones is less than 7 percent.

In Fig. 5 we compare the saturation profile of CO_2 along the macroscopic direction x of flow at the breakthrough time t_B, where $X = x/L$, with L being the linear size of the image. The saturation was computed for each plane at position X perpendicular to the direction of macroscopic flow. The agreement is excellent.

Fig. 6 presents the evolution with time t_D of CO_2 saturation S_{CO_2} in the original image of the porous medium, and compares it with those computed with the thresholded images, where $t_D = t/t_B$, with t being the actual time. At short times the three profiles are identical. At longer times, all the way to the breakthrough time, the maximum difference the profile with $\epsilon = 0.9$ and the original image is about 3 percent.

Fig. 7 makes a comparison between the relative permeabilities K_r of the two fluids that were computed in the original image of Berea sandstone and those calculated with the thresholded images. The agreement is excellent in all the cases, indicating the accuracy of the computations with the thresholded images.

To understand the excellence of the accuracy of the computed relative permeabilities, we present in Fig. 8 the distribution of local flow velocities in the original image of the sandstone with those computed with the thresholded images, where we have normalized the velocities by their maximum value. Fig. 8 indicates that for velocities up to the maximum of the distributions, the agreement between all the distributions is perfect. Beyond the maximum, the agreement is good, with all the distributions having the same shape and almost identical tails.

An important quantity in two-phase flow in porous media is the residual saturation S_{br} of the displaced fluid (brine in the present simulation), its saturation at the CO_2 breakthrough point. In Table 1 we compare the computed residual saturations in the original image and its thresholded counterparts. The maximum difference, computed with $\epsilon = 0.9$, between the residual saturations in the original image and the thresholded one is 7.5 percent.

6. Speed-up of the computations

We used 2D CT in order to denoise the 3D image, for which the computational cost of a digitized image of size $n \times n$ is $\mathcal{O}(n^2 \log n)$. For the 2D slices of size 200^2 pixels the CPU time is very small, but since

Table 1
Comparison of the number of grid blocks N, the computation times, and the brine residual saturation S_{br}, computed with the original and curvelet transform-thresholded images. The CPU times represent those for simulating the two-phase flow.

Sandstone	N	Threshold ε	S_{br}	Time (CPU sec)
Original image	3,346,168		0.388	144,231
Curvelet-transformed image	15,005	0.5	0.408	547
Curvelet-transformed image	11,996	0.9	0.417	489

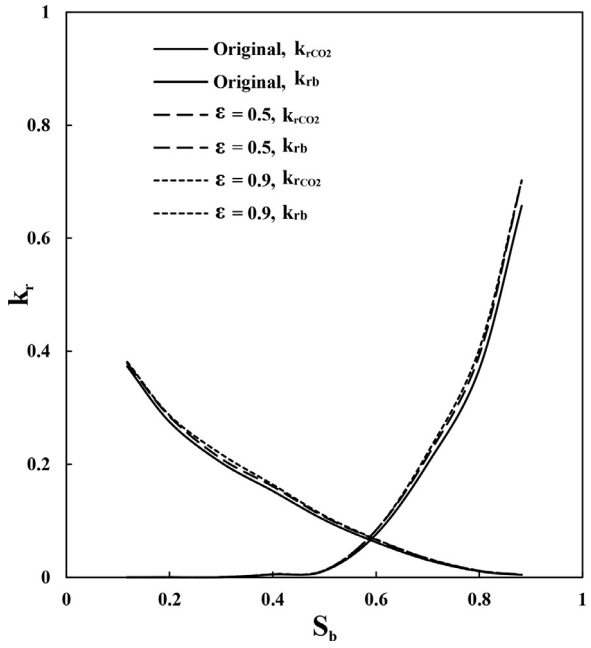

Fig. 7. CO_2-brine relative permeability curves, as function of the brine saturation S_b in the sandstone's original image, and their comparison with those computed with the curvelet-thresholded images.

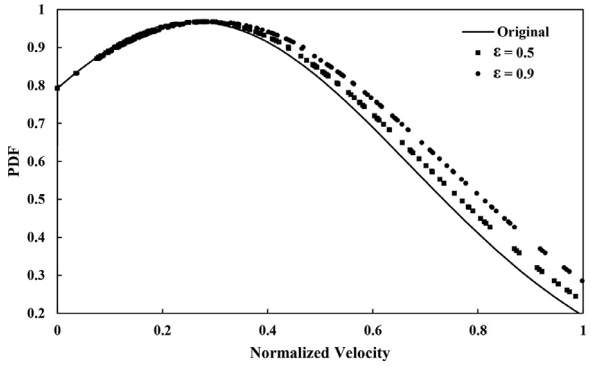

Fig. 8. The probability density function (PDF) of the local (pore) velocity of CO_2, normalized by the maximum flow velocity, in the curvelet-transformed images of the Sandstone with two thresholds ε, and their comparison with those in the original image.

we denoise a large number of them, the computation time is relatively significant (see below). Stacking the 200 denoised slices took only 82 CPU seconds.

In Table 1 we compare the details of the computations: the total number N of grid blocks, the CPU times for all the cases, and the brine residual saturations.

We note that even the computed results with the denoised image with a threshold $\varepsilon = 0.9$ are still very accurate, and differ from those of the original images by at most 7 percent. Moreover, the speed-up factors for the computations with the thresholds $\varepsilon = 0.5$ and 0.9 are, respectively, 263 and 294. These speed-up factors are for simulating the two-phase flow problem. If we add the CPU time for denoising the 2D slices and reconstructing a coarser 3D image to the CPU time for simulating the flow problem, then the speed-up factor is about one order of magnitude, a factor of 7–10, which is still very significant. Note, however, that the denoising is done only once, while the denoised image can be used in the simulation of a variety of processes in the same image.

The reason for the very significant speed-up is removal of the redundant information from the image, which makes it possible to use a coarser computational grid. After the image is denoised, one must no longer use a highly resolved computational grid everywhere, but only in selected areas that are determined by the CT. This includes parts of the pores, as the difference between their CCs and those of the neighbors and in the solid phase is large and, moreover, they are also correlated with the areas next to the interface between the pores and the matrix.

Can the efficiency of image-based simulation of two-phase flows in porous media be increased by other methods? It can, of course, be increased, but we are not aware of any method that uses a single processor and achieves the order of the speed-uop in the computations that we report while preserving the accuracy, based on a transformation whose mathematical foundation is rigorous and was developed precisely for curvy complex space and, specifically, for image processing.

According to Ying et al. (2005), a 256^3 grid takes 250 CPU seconds to be curvelet transformed by a 3D curvelet. This does not include its thresholding (which is insignificant), and inverse transforming its coarser version. Despite this, direct use of 3D CT for denoising a 3D image results in even better speed-up factors than what we obtained here, even after adding the time of the image processing to the cost of simulating the flow problem. We will report on this aspect in the near future.

7. Summary

With the rapid increase in the speed of computations and significant advances in instrumentations it has become possible to simulate multiphase flows in 2D and 3D images of heterogeneous porous media. As image-based simulation of multiphase flow in heterogeneous porous media becomes more practical, one must, however, address the issue of high computational cost for such simulations, while a variety of methods have been proposed, such as use of graphics processing units (GPUs), and parallel computations using multiple processors, we described in this paper a new methodology to address the issue. The approach is based on curvelet transforming the image and processing it by removing those details that do not contribute significantly to physics of fluid flow. The computations in the less noisy and coarser images yield results that are as accurate as those in the original ones, but with a very large speed-up factor. This was demonstrated by simulation of two-phase flow of CO_2 and brine in the 3D images of a sandstone. All the properties of the two-phase flow system, computed with the CT-processed images were in excellent agreement with those computed with the original resolved image. Thus, the methodology represents a significant step toward achieving the ultimate goal of direct image-based simulations of two-phase flows based on the governing equations, namely, making such simulations a standard practice.

Author Statement

Sahimi conceived the idea. Sahimi and Aljasmi designed the solution. Aljasi did the computations. Sahimi and Aljasmi analyzed the results. Sahimi wrote the paper. Funding was provided by the NSF as the senior investigator.

Declaration of Competing Interest

The authors declare that they have no known competing financial interests or personal relationships that could have appeared to influence the work reported in this paper.

Acknowledgments

A.A. is grateful to the Public Authority for Applied Education and Training of Kuwait for a Ph.D. scholarship. This work was also supported in part by the National Science Foundation Grant CBET 2000968.

References

Aljasmi, A., Sahimi, M., 2020. Efficient image-based simulation of flow and transport in heterogeneous porous media: application of curvelet transforms. Geophys. Res. Lett. 47. e2019GL085671

An, S., Zhan, Y., Yao, J., Yu, H.W., Niasar, V., 2020. A greyscale volumetric lattice Boltzmann method for upscaling pore-scale two-phase flow. Adv. Water Resour. 144, 10711.

Andrew, M., Menke, H., Blunt, M.J., Bijeljic, B., 2015. The imaging of dynamic multiphase fluid flow using synchrotron-based x-ray microtomography at reservoir conditions. Transp. Porous Media 110, 1–24.

Arns, C.H., Knackstedt, M.A., Pinczewski, W.V., Garboczi, E., 2002. Computation of linear elastic properties from microtomographic images: methodology and agreement between theory and experiment. Geophysics 67, 1348–1672.

Arns, C.H., Knackstedt, M.A., Pinczewski, W.V., Lindquist, W.B., 2001. Accurate computation of transport properties from microtomographic images. Geophys. Res. Lett. 28, 3361–3364.

Babaei, M., King, P.R., 2011. A comparison between wavelet and renormalization upscaling methods and iterative upscaling-downscaling scheme. SPE Reservoir Simul. Symp. 1, 469.

Bakhshian, S., Shi, Z., Sahimi, M., Tsotsis, T.T., Jessen, K., 2018. Image-based modeling of gas adsorption and swelling in high-pressure porous formations. Sci. Rep. 8, 8249.

Bear, J., 1972. Dynamics of Fluids in Porous Media. Dover, Mineola.

Berg, S., Ott, H., Klapp, S.A., Schwing, A., Neiteler, R., Brussee, N., Makurat, A., Leu, L., Enzmann, F., Schwarz, J.-O., Kersten, M., Irvine, S., Stampanoni, M., 2013. Real-time 3D imaging of haines jumps in porous media flow. Proc. Natl. Acad. Sci. U.S.A. 110, 3755.

Blunt, M.J., 2017. Multiphase Flow in Permeable Media: A Pore-Scale Perspective. Cambridge University Press, Cambridge.

Candés, E., Demanent, L., Donoho, D.L., Ying, L., 2005. Fast discrete curvelet transforms. Multiscale Model. Simul. 5, 861.

Dashtian, H., Sahimi, M., 2014. Coherence index and curvelet transformation for denoising geophysical data. Phys. Rev. E 90, 042810.

Daubechies, I., 1988. Orthonormal basis of compactly supported wavelets. Commun. Pure Appl. Math. 41, 901.

Daubechies, I., 1992. Ten Lecture on Wavelets. SIAM, Philadelphia.

Donoho, D.L., 1999. Wedgelets: nearly minimax estimation of edges. Ann. Stat. 27, 859.

Ebrahimi, F., 2010. Invasion percolation: a computational algorithm for complex phenomena. Comput. Sci. Eng. 12 (2), 84.

Ebrahimi, F., Sahimi, M., 2002. Multiresolution wavelet coarsening and analysis of transport in heterogeneous porous media. Physica A 316, 160.

Ebrahimi, F., Sahimi, M., 2004. Multiresolution wavelet scale up of unstable miscible displacements in flow through porous media. Transp. Porous Media 57, 75.

Etemad, S., Behrang, A., Mohammadmoradi, P., Hejazi, S.H., Kantzas, A., 2017. Effects of surface roughness and mineral heterogeneity on pore-scale steam condensation. J. Pet. Sci. Eng. 159, 624.

Francois, M.M., Cummins, S.J., Dendy, E.D., Kothe, D.B., Sicilian, J.M., Williams, M.M., 2006. A balanced-force algorithm for continuous and sharp interfacial surface tension models within a volume tracking framework. J. Comput. Phys. 213, 141.

Friedlingstein, P., Solomon, S., 2005. Contributions of past and present human generations to committed warming caused by carbon dioxide. Proc. Natl. Acad. Sci. U.S.A. 102, 10832.

Ghanbarian, B., Sahimi, M., Daigle, H., 2016. Modeling relative permeability of water in soil: application of effective-medium approximation and percolation theory. Water Resour. Res. 52, 5025.

Grinsted, A., Moore, J.C., Jevrejeva, S., 2004. Application of the cross wavelet transform and wavelet coherence to geophysical time series. Nonlinear Processes Geophys. 11, 561.

Gueyffier, D., Li, J., Nadim, A., Scardovelli, R., Zaleski, S., 1999. Volume-of-fluid interface tracking with smoothed surface stress methods for three-dimensional flows. J. Comput. Phys. 152, 423.

Helmig, R., 1997. Multiphase Flow and Transport Processes in the Subsurface. Springer, Berlin.

Herrmann, F.J., Wang, D., Hennenfent, G., Moghaddam, P.P., 2007. Curvelet-based seismic data processing: a multiscale and nonlinear approach. Geophysics 73, A1.

Huang, H., Sukop, M., Lu, X., 2015. Multiphase Lattice Boltzmann Methods: Theory and Application. Wiley, New York.

Hunt, A.G., Sahimi, M., 2017. Flow, transport, and reaction in porous media: percolation scaling, critical-path analysis, and effective-medium approximation. Rev. Geophys. 55, 993.

Iglauer, S., Favretto, S., Spinelli, G., Schena, G., Blunt, M.J., 2010. X-ray tomography measurements of power-law cluster size distributions for the nonwetting phase in sandstones. Phys. Rev. E. 82, 056315.

Kantzas, A., Chatzis, I., 1988. Network simulation of relative permeability curves using a bond correlated-site percolation model of pore structure. Chem. Eng. Commun. 69, 1.

Kantzas, A., Marentette, D.F., Jha, K.N.N., 1992. Computer-assisted tomography: from qualitative visualization to quantitative core analysis. J. Can. Pet. Technol. 31. PET-SOC-92-09-06

Knackstedt, M.A., Sheppard, A.P., Sahimi, M., 2001. Pore network modeling of two-phase flow in porous rock: the effect of correlated heterogeneity. Adv. Water Resour. 24, 257.

Kohanpur, A.H., Rahromostaqim, M., Valocchi, A.J., Sahimi, M., 2020. Two-phase flow of CO_2-brine in a heterogeneous sandstone: characterization of the rock and comparison of the lattice-Boltzmann, pore-network, and direct numerical simulation methods. Adv. Water Resour. 135, 103439.

Kumar, P., Foufoula-Georgiou, E., 1997. Wavelet analysis for geophysical applications. Rev. Geophys. 35, 385–412.

Lemmens, H.J., Butcher, R., Botha, P.W.S.K., 2011. FIB/SEM and SEM/EDX: a new dawn for the SEM in the core lab? Petrophysics 52, 452.

Ma, J., Plonka, G., 2009. Computing with curvelets: from image processing to turbulent flows. Comput. Sci. Eng. 11 (2), 72.

Mallat, S.G., 1989. Multiresolution approximations and wavelet orthonormal bases of $l^2(r)$. Trans. Am. Math. Soc. 315, 69.

Mallat, S.G., 1989. A theory for multiresolution signal decomposition: the wavelet representation. IEEE Trans. Pattern Recog. Machine Intell 11, 674.

Mehrabi, A.R., Sahimi, M., 1997. Coarsening of heterogeneous media: application of wavelets. Phys. Rev. Lett. 79, 4385.

Metz, B., Davidson, O., De Coninck, H., 2005. Carbon Dioxide Capture and Storage: Special Report of the Intergovernmental Panel on Climate Change. Cambridge University Press, London.

Neelamani, R., Baumstein, A.I., Gillard, D.G., Hadidi, M.T., Soroka, W.L., 2008. Coherent and random noise attenuation using the curvelet transform. Leading Edge 27, 129.

Nordbotten, J.M., Celia, M.A., 2011. Geological Storage of CO_2: Modeling Approaches for Large-Scale Simulation. Wiley, New York.

Olhede, S., Walden, A.T., 2004. The hilbert spectrum via wavelet projections. Proc. R. Soc. Lond. A 460, 955.

Pancaldi, V., Christensen, K., King, P.R., 2007. Permeability up-scaling using haar wavelets. Transp. Porous Media 67, 395.

Piller, M., Schena, G., Nolich, M., Favretto, S., Radaelli, F., Rossi, E., 2009. Analysis of hydraulic permeability in porous media: from high resolution x-ray tomography to direct numerical simulation. Transp. Porous Media 80, 57.

Piri, M., Blunt, M.J., 2005. Three-dimensional mixed-wet random pore-scale network modeling of two–and three–phase flow in porous media. II. Results. Phys. Rev. E 71, 026302.

Porter, M.L., Wildenschild, D., Grant, G., Gerhard, J.I., 2010. Measurement and prediction of the relationship between capillary pressure, saturation, and interfacial area in a NAPL-water-glass bead system. Water Resour. Res. 46, W08512.

Raeini, A.Q., 2013. Modelling multiphase flow through micro-CT images of the pore space. Imperial College of London Ph.D. thesis.

Raeini, A.Q., Blunt, M.J., Bijeljic, B., 2012. Modelling two-phase flow in porous media at the pore scale using the volume-of-fluid method. J. Comput. Phys. 231, 5653.

Raeini, A.Q., Blunt, M.J., Bijeljic, B., 2014. Direct simulations of two-phase flow on micro-CT images of porous media and upscaling of pore-scale forces. Adv. Water Resour. 74, 116.

Ramstad, T., Idowu, N., Nardi, C., Oren, P.E., 2012. Relative permeability calculations from two-phase flow simulations directly on digital images of porous rocks. Transp. Porous Media 94, 487–504.

Rasaei, M.R., Sahimi, M., 2008. Upscaling and simulation of waterflooding in heterogeneous reservoirs using wavelet transformations: application to the SPE-10 model. Transp. Porous Media 72, 311.

Rasaei, M.R., Sahimi, M., 2009. Upscaling of the permeability by multiscale wavelet transformations and simulation of multiphase flows in heterogeneous porous media. Comput. Geosci. 13, 187.

Rezapour, A., Ortega, A., Sahimi, M., 2019. Upscaling of geological models of oil reservoirs with unstructured grids using lifting-based graph wavelet transforms. Transp. Porous Media 127, 661.

Sahimi, M., 2011. Flow and transport in porous media and fractured rock, second ed. Wiley-VCH, Weinheim.

Sahimi, M., Hashemi, M., Ghassemzadeh, J., 1998. Site-bond invasion percolation with fluid trapping. Physica A 260, 231–243.

Sahimi, M., Heiba, A.A., Davis, H.T., Scriven, L.E., 1986. Dispersion in flow through porous media: II. Two-phase flow. Chem. Eng. Sci. 41, 2123–2136.

Schindelin, J., Arganda-Carreras, I., Frise, E., Kaynig, V., Longair, M., Pietzsch, T., Preibisch, S., Rueden, C., Saalfeld, S., Schmid, B., 2012. Fiji: an open-source platform for biological-image analysis. Nat. Methods 9, 676.

Sheppard, S., Mantle, M.D., Sederman, A.J., Johns, M.L., Gladden, L.F., 2003. Magnetic resonance imaging study of complex fluid flow in porous media: flow patterns and quantitative saturation profiling of amphiphilic fracturing fluid displacement in sandstone cores. Magn. Reson. Imaging. 21 (365), 2003.

Shinde, A.A., Rahulkar, A.D., Patil, C.V., 2017. Fast discrete curvelet transform-based anisotropic feature extraction for biomedical image indexing and retrieval. Int. J. Multimed. Inf. Retrieval 6, 281–288.

Starck, J.-L., Candés, E.J., Donoho, D.L., 2002. The curvelet transform for image denoising. IEEE Trans. Image Process. 11 (6), 670.

Tahmasebi, P., Sahimi, M., Kohanpur, A.H., Valocchi, A.J., 2017. Pore-scale simulation of flow of CO_2 and brine in reconstructed and actual 3D rock cores. J. Pet. Sci. Eng. 155, 21.

Ubink, O., 1997. Numerical prediction of two fluid systems with sharp interfaces. Imperial College of London Ph.D. Thesis.

Valvatne, P.H., Blunt, M.J., 2004. Predictive pore-scale modeling of two-phase flow in mixed wet media. Water Resour. Res. 40, W07406.

Wildenschild, D., Armstrong, R.T., Herring, A.L., Young, I., Young, I.M., Carey, J.W., 2014. Exploring capillary trapping efficiency as a function of interfacial tension, viscosity, and flow rate. Energy Procedia 4, 4945.

Woiselle, A., Starck, J.-L., Fadili, J., 2010. 3D curvelet transforms and astronomical data restoration. Appl. Comput. Harmonic 28, 171.

Ying, L., Demanet, L., Candés, E., 2005. 3D discrete curvelet transform. In: Proc. SPIE5914, Wavelets XI, p. 591413.